Nanoscale

PAPER

View Article Online
View Journal | View Issue

Check for updates

Cite this: *Nanoscale*, 2019, **11**, 16844

Silicon nanomembrane-based near infrared phototransistor with positive and negative photodetections†

Ruobing Pan,[a] Qinglei Guo,[b] Jun Cao,[c] Gaoshan Huang, [a] Yang Wang,[a] Yuzhou Qin,[a] Ziao Tian,[d] Zhenghua An,[c] Zengfeng Di[d] and Yongfeng Mei *[a]

Received 19th June 2019,
Accepted 18th August 2019

DOI: 10.1039/c9nr05189a

rsc.li/nanoscale

Surface plasmon polariton induces hot carrier injection that enables near infrared photodetection in Si nanomembranes and is of great significance for Si photonics integrated circuits. In this study, near infrared photodiode and phototransistor based on Si nanomembranes are designed and demonstrated, where the channel carrier concentration can be tuned through a gate modulation to implement both positive and negative photodetections. Through patterning a nanogroove array, Si nanomembrane-based photodetector exhibits high performance in near infrared range with an I_{on}/I_{off} ratio of 10^2, and a responsivity of 7 mA W^{-1}, under 1550 nm laser irradiation. Moreover, the photodetection ability, determined by I_{off}/I_{on} can be further enhanced to ~6 × 10^2 when the photodetector is modulated to work at the negative photodetection mode. Our study may provide a practical approach with fundamental guidelines and designs for fabricating high-performance Si-based infrared photodetection, which promotes the development of Si photonics.

Introduction

Recent advances in Si photonics lay the foundation for highly dense integration of various functional devices on a chip, such as lasers, waveguides, photomodulators, and photodetectors, which offer enormous opportunities in future wireless, remote radio frontend and detection.[1–3] Driven by the tendency of the telecom and/or optical communications, a near infrared (NIR) photodetector is considered as one of the mostly demanded components of photonic integrated chip. Conventional semiconductors with a small band gap, such as germanium or III–V alloy,[4–6] have been utilized to fabricate NIR photodetectors. However, the susceptible surface property of germanium[7] and the incompatibility with the CMOS technology of III–V[8] materials would become obstacles for the further development of NIR photodetectors. Si is naturally compatible with CMOS technology, and also possesses stable physical properties.[6,9–12] Although its intrinsic band gap (1.12 eV) makes Si "transparent" to the NIR waveband, realizing the NIR photodetection in Si will surely give significant potentials for Si photonics.

In order to achieve the NIR photodetection in Si, various approaches have been demonstrated, including the combination with graphene, transition metal dichalcogenides,[13] and surface states.[14–16] Among these, designs and principles based on surface plasmon polariton (SPP) are considered as a practical way due to their compatible CMOS fabrication process and controllable and attainable superior performances of NIR photodetectors.[17] By introducing various nanostructures with sub-wavelength sizes, such as nanohole array,[18] grating,[12] and nanogroove,[19] the incident NIR light can be localized within these nanostructures and resonate strongly with matter to generate hot carrier injections, resulting in an exceptional NIR photoresponse in Si. Previous studies about SPP induced NIR photodetection in Si are mainly focused on obtaining a lower power consumption, polarization-insensitive detection,[18] or stable performances.[20] However, moderate optoelectronic performances, including photodetection ability (determined by the I_{on} and I_{off}) and responsivity, are still the main issues that should be addressed.[21,22]

In this article, we demonstrate a SPP induced high-performance Si-based NIR phototransistor, in which both the positive and negative photodetections were realized *via* the gate modu-

[a] *Department of Materials Science, State Key Laboratory of ASIC and Systems, Fudan University, Shanghai 200433, People's Republic of China. E-mail: yfm@fudan.edu.cn*
[b] *Center of Nanoelectronics and School of Microelectronics, Shandong University, Jinan 250100, P. R. China*
[c] *Department of Physics, Fudan University, Shanghai 200433, People's Republic of China*
[d] *State Key Laboratory of Functional Materials for Informatics, Shanghai Institute of Microsystem and Information Technology, Chinese Academy of Sciences, Shanghai 200050, People's Republic of China*
† Electronic supplementary information (ESI) available. See DOI: 10.1039/c9nr05189a

lation. The phototransistors could break through the limitation of lower carrier injection efficiency of a two-terminal detection device. Large detection window and high responsivity were achieved in this work. While with a floating gate, the I_{on}/I_{off} ratio and responsivity of two-terminal devices are obtained in the order of 10^2 and 7 mA W^{-1}, respectively. Moreover, the generation of hot hole injection and transportation mechanism were deeply investigated through theoretical predictions and calculations. On the other hand, under gate bias modulation, a deep insight investigation concerning the hot hole injection was carried out. The presented results and demonstrations in this work may provide guidelines and fundamentals in designing and fabricating high-performance Si based NIR photodetectors, which offer numerous opportunities for the development of Si photonics.

Results and discussion

Fabrication of Si based NIR photodetectors begins with defining nanostructures in Si. As shown in Fig. 1a, a cleaned silicon on insulator (SOI, resistivity: 10 Ω cm) with a p-type, 200 nm-thick top Si nanomembrane is patterned into nanogroove structures. The detailed fabrication process can be found in the Experimental section. For each unit of nanogroove array, the area is defined as 85 μm × 100 μm. Then, 2 nm Ti and 15 nm Au are deposited by magnetron sputtering to get smooth and compact absorption objects. A previous study

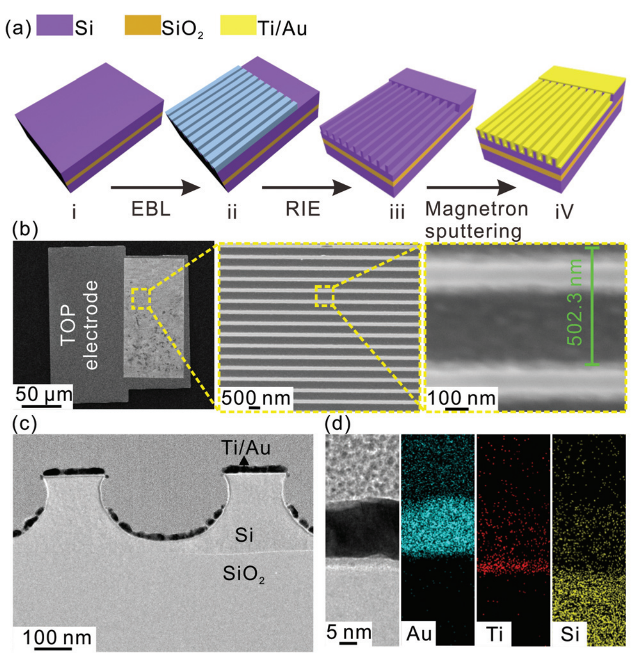

Fig. 1 Fabrication and structures of nanogroove-structured Si nanomembrane. (a) Schematic of the microfabrication process using EBL, RIE, and magnetron sputtering. (b) SEM image of the device and enlarged images of a nanogroove. (c) TEM image of the cross section of a nanogroove. (d) Element mapping for the evaporated stack of materials (Au 15 nm and Ti 2 nm).

demonstrated that the thickness of a metal film for SPP should be no larger than the hot carrier propagation distance in order to reach high photoresponsivity and high hot carrier collection efficiency.[23] The propagation distances of hot carriers in metal (δ_m) and dielectric (δ_d) layers can be related as per the following eqn (1) and (2),[24]

$$\delta_d = \frac{1}{k_0}\left|\frac{\varepsilon_d + \varepsilon'_m}{{\varepsilon_d}^2}\right|^{1/2} \tag{1}$$

$$\delta_m = \frac{1}{k_0}\left|\frac{\varepsilon_d + \varepsilon'_m}{{\varepsilon'_m}^2}\right|^{1/2} \tag{2}$$

where k_0 is the wave vector in vacuum, ε_d is the dielectric constant of dielectric layer, and ε'_m is the real part of metal dielectric constant. To extend the photoresponse spectrum of Si into the NIR region, the momentum of hot holes should be much larger than the Schottky barrier height, and be lower than the Si band gap.[25,26] Therefore, Ti, which is capable of enhancing the adhesion between Au and Si, is chosen to form a low barrier height Schottky contact with the p-type Si to ensure efficient hot carrier injections.[26,27] According to the following equation,[28]

$$\frac{\sqrt{{k_x}^2 - {k_0}^2}}{k_0} = \frac{a}{d}\tan k_0 h \tag{3}$$

where, h, a, and d denote the depth, width and constant of period of the designed nanogroove, respectively, whereas k_x is the wave vector of SPP, and k_0 is the incident wave vector in vacuum; we design the nanogroove with the width a changing from 325 to 470 nm, as shown in Fig. S1.† For all nanogrooves with different widths, the depth h and period constant d are kept as 180 nm and 500 nm, respectively. The surface morphology of the NIR photodetector is characterized by scanning electron microscopy (SEM). As shown in Fig. 1(b), the nanogroove array has a sub-wavelength size of period constant, which will be beneficial for localizing the incident optical wave. Fig. 1(c) shows the cross-sectional view of the device by transmission electron microscopy (TEM), and the element mapping results shown in Fig. 1(d) clearly illustrate the metal layers (Ti and Au) for SPP and the functional layer (Si) for photodetection.

For a photodetection device, the absorption spectrum plays a vital role in its optoelectronic performances. In this spirit, nanogroove size-dependent absorption of a Si based NIR photodetector is evaluated by the Fourier transform infrared spectrometer (FTIR). The absorption A is defined as $A = 1 - R - T$, where R and T are reflection and transmission, respectively. Detailed results of the reflection and transmission spectra are shown in Fig. S2(a) and S2(b).† As shown in Fig. 2(a), absorption spectra obtained from the device with the nanogroove width varying from 325 to 470 nm contain two groups of peaks. The peaks around 1100 nm are attributed to thin film interference arising from multiple reflections between top Si and buried oxide of SOI.[23,25,29] Another group of absorption peaks located within 1480–1800 nm are gener-

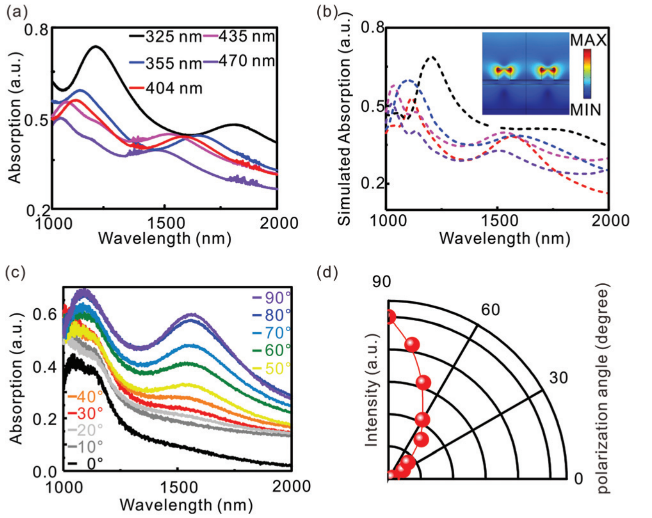

Fig. 2 Optical properties of Si nanomembranes with various nanogrooves. (a) Experimental results of the absorption spectra of Si nanomembranes with different nanogroove widths. (b) Simulated results of the absorption spectra of Si nanomembranes with different nanogrooves. The peak around 1500 nm exhibits a red shift as the width of nanogroove increases. (c) Light absorption spectra of a typical Si nanomembrane with a nanogroove width of 403 nm under illumination with different polarization angles. (d) The intensity of the absorption peak (1530 nm) as a function of the polarization angle.

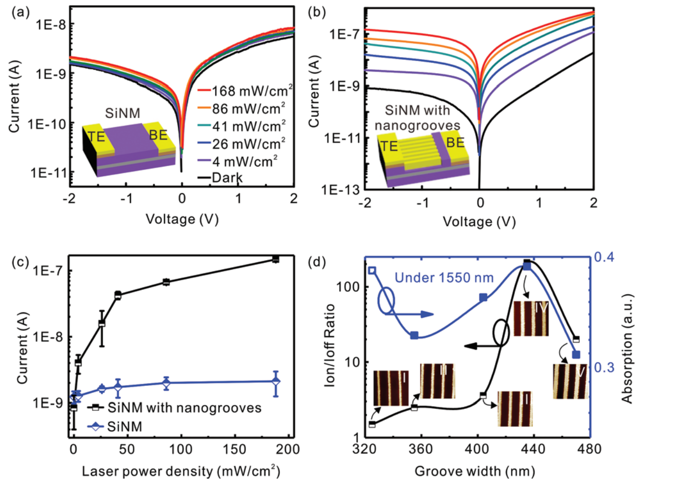

Fig. 3 Electrical characterization of SPP induced Si based NIR photodiode. (a) I–V characteristics of a smooth Si nanomembrane based photodiode under dark and 1550 nm irradiation. (b) I–V characteristics of a Si nanomembrane based photodiode with nanogroove structures under dark and 1550 nm irradiation. (c) Photocurrent extracted from (a) and (b) as a function of laser power density. (d) Experimental results of the I_{on}/I_{off} ratio (black) and light absorption (blue) varying with the nanogroove width. AFM images of the nanogroove with different widths are shown in the inset.

ated from the SPP resonance by artificial nanogrooves. Moreover, as the width of the nanogroove decreases, a redshift of the peak is found. These experimental observations are further verified by numerical analysis. As shown in Fig. 2(b), the simulated results of the absorption spectra, obtained by FEM software (finite element methods), are in good agreement with the experiments. Furthermore, typical F–P resonance enhances the near field localization,[19] as demonstrated in the inset of Fig. 2(b), indicating a successful SPP resonance induced by nanogroove structures.

Further demonstration of the existence of SPP resonance is revealed by the polarization dependence of the absorption spectra. Taking the device with the 404 nm width nanogroove as an example, the absorption spectra under illumination with different polarization angles are measured. As shown in Fig. 2(c), the intensity of the intrinsic absorption peak (around 1100 nm) has no significant variation under different rotation angles. For the absorption peak around 1530 nm, however, the peak intensity gradually decreases to zero as the polarization angle reduces from 90° to 0°. The statistical details about the peak intensity varying with the polarization angle are illustrated in Fig. 2(d). From these presented results, one can speculate that only transverse magnetic mode (TM mode) propagation exists, which confirms that the sub-bandgap absorption is generated from the SPP resonance but not the interference.[30]

With the capability of NIR absorption in the nanogroove structured Si nanomembranes, their corresponding photodetectors are fabricated and characterized. A counterpart of photodetector based on the Si nanomembrane without any pattern is measured for comparison. As shown in Fig. 3(a), under the 1550 nm laser irradiation with different power densities, photocurrents obtained from the Si nanomembrane based photodetector exhibit no significant change due to its poor sub-band gap absorption. In contrast, photocurrents obtained from the photodetector, fabricated with nanogroove patterned Si nanomembranes (nanogroove width: 435 nm), increase distinctly as the power density of the 1550 nm laser increases, as displayed in Fig. 3(b). We attribute this exceptional NIR response to the hot hole injection induced by SPP resonance. I_{on}/I_{off} ratios as a function of the power density measured from the photodetectors with smooth Si nanomembrane and with nanogroove-structured Si nanomembrane are summarized in Fig. 3(c). The bias voltage is set as −2 V, and the power density of the 1550 nm laser is gradually tuned from 4 to 168 mW cm^{-2}. It should be noted that for the nanogroove-structured Si nanomembrane-based photodetector, the ratio of photocurrent to dark current can reach about two orders of magnitude and the responsivity is 7 mA W^{-1}. Other photodetectors with different widths of nanogroove are characterized, and the detailed I–V curves with/without light illumination are shown in Fig. S3.† Fig. 3(d) displays the I_{on}/I_{off} ratio and the light absorption (at 1550 nm) varying with the nanogroove width. When the width of the nanogroove is 435 nm, the I_{on}/I_{off} ratio reaches the maximum value, which is consistent with the light absorption results. Moreover, the hollow square represents 325 nm groove width, which exhibits a high absorption at 1550 nm, but the on/off ratio for this photodetection device is small. Its high absorption intensity at 1550 nm can be mainly attributed to the interference rather than the SPP, which cannot contribute to the light-generated carrier injection for photocurrent enhancement. The corresponding response rate and the detailed performance comparison are shown in ESI.†

The ability of a photo detector to sense light in a wide range offers promising opportunities for its further applications. Therefore, optoelectronic responses of the Si nanomembrane based NIR photodetectors to the broadband spectrum from 770 to 1450 nm is investigated, as shown in Fig. 4(a) and (b). After the Si nanomembranes are patterned with nanogroove structures, drastic enhancements in both photocurrent and responsivity are observed, especially for the device with a nanogroove width of 435 nm. At the sub-bandgap photon energy wavelength region (1100–1400 nm), the enhancement is generated from the inter-band excitation and hot carrier injection.

It is known that the transistor with a gate terminal has the ability of modulating the current passing through the channel, thus exhibiting characteristics similar to those of an amplifier. Motivated by this, we fabricated phototransistors on Si nanomembranes with nanogroove structures, and the performance was characterized. A typical transfer curve is presented in Fig. 5(a); the on-state current is about 10^{-5} A as depicted in the transfer curve in both semi-log and linear scale. The drain voltage (V_{DS}) is kept as 2 V, and the on/off ratio reaches about 10^4. With contact optimization, the maximal on/off ratio can reach up to 10^5 (see Fig. S5†). The effective channel mobility is calculated to be about 380 cm^2 V^{-1} s^{-1}. Detailed calculation method can be found in ESI.† Fig. 5(b) presents the output curves of the phototransistor at various gate bias voltages from +10 to +2 V.

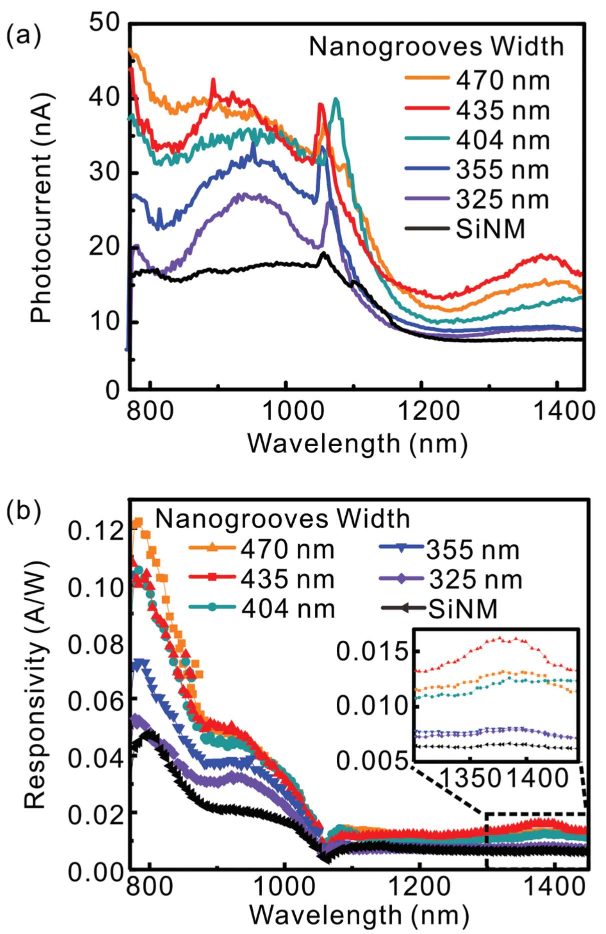

Fig. 4 Optoelectronic performances of Si nanomembrane based photodiode without/with nanogrooves. (a) Photocurrent spectra obtained from all types of photodiodes. (b) Responsivity spectra obtained from all types of photodiodes. The responsivity locating with 1300–1450 nm is magnified at the top-right, indicating an apparent NIR response.

Once irradiated by a 1550 nm laser, the phototransistor exhibits a drastic negative photoconductance. As shown in Fig. 5(c), a decrease in the photocurrent, which is regarded as negative photoconductance,[31] is obtained from the phototransistor with a zero gate voltage (red line) compared with that obtained from the phototransistor with a floating gate (black line). This relative decrease in the photocurrent is magnified under gate bias modulation. Fig. 5(d) shows the transfer curve of the phototransistor measured with different illumination power densities. Under the 1550 nm illumination, with the power density varying from 26 to 86 mW cm^{-2}, the on-state current decreased by more than two orders of magnitude compared to that obtained from dark condition. As the incident light power increases, the on-state current reduces to about 10^{-8} A, and the photodetection ability (herein defined as I_{off}/I_{on}) reaches up to 6 × 10^2, suggesting a good signal to noise ratio of the Si based NIR phototransistors induced by SPP. Once the illuminated light is turned off, the on-state current (labelled as "light off" in Fig. 5(d)) recovers to its initial state (labelled as "dark"). Considering that the utilized p-type Si nanomembrane offers an n-type channel at the switch-on status, the hot hole injection induced by SPP resonance during the NIR light illumination consumes the electrons existing in the channel, resulting in a decrease in the carrier concentration of the channel and leading to a decreased on-state current. For the reverse cut-off current, however, a slight increase with the increase in the illumination power density is found, as shown in Fig. 5(e). It is known that the reverse cut-off current is determined by the hole transportation under a negative gate bias. Hence, the increase in the reverse cut-off current, though having no direct impact on the performance of the phototransistor, results from the hot hole injection induced by SPP.

In addition to the photocurrent, the threshold voltage also indicates a light illumination-dependent behaviour, as shown in Fig. 5(f). The threshold voltage, extracted from the V_G–I_{DS} curve, exhibits a gradual decrease as the illumination power density increases. A previous study demonstrated that the threshold voltage of phototransistor was closely related to the carrier concentration.[32] These observations further prove the ability of the SPP resonance in tuning the carrier concentration of Si nanomembranes. Other transfer characteristics of Si based phototransistors with different nanogroove widths are also measured under dark as well as illumination conditions, and the results are shown in Fig. S6.†

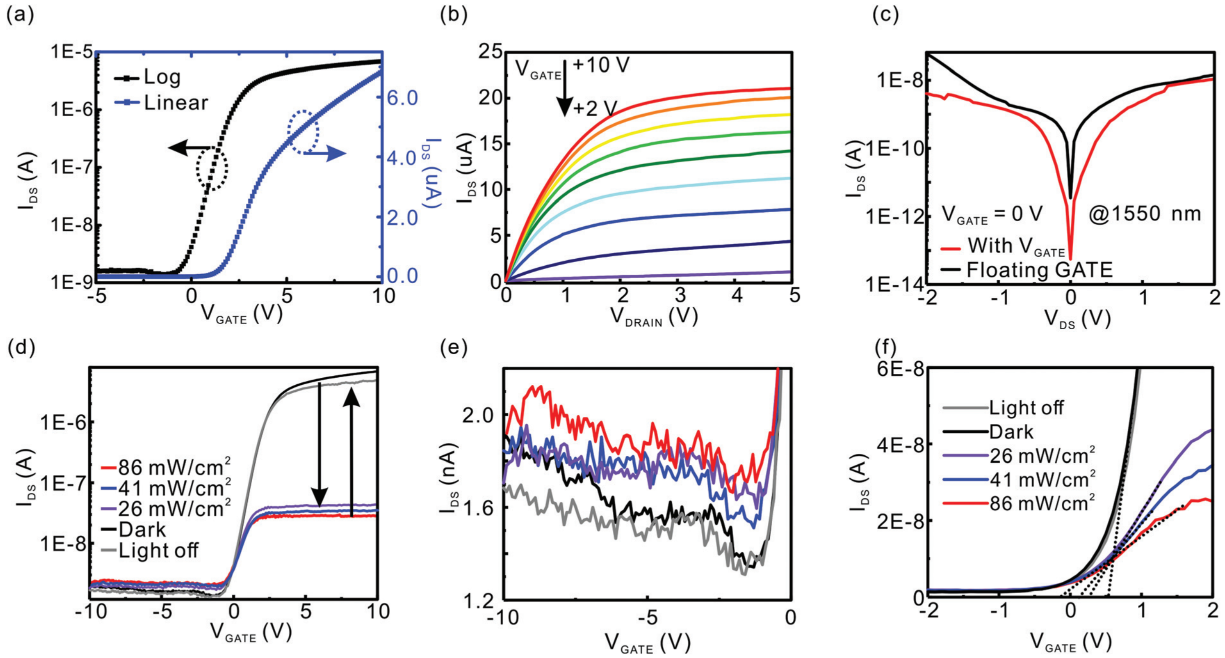

Fig. 5 Optoelectronic properties of Si nanomembrane based phototransistors with nanogroove structures. (a) Transfer curve of the phototransistor in both semi-logarithmic and linear coordinate under dark at a V_{DS} of 2 V. (b) Output curves for the phototransistor. (c) *I*–*V* characteristics of the device without a gate (*i.e.*, floating gate) and with a gate (gate voltage = 0 V) under a 1550 nm light illumination. (d) Transfer characteristics with gate voltage sweeping from −10 to 10 V under various power densities. (e) Magnified cut-off current region under negative gate bias. (f) Threshold voltage depicted by the tangent line (dotted line) of transfer curves.

In order to deeply understand the mechanism of the negative photo conductance of the SPP induced Si based NIR phototransistors, band alignments under different bias and illumination conditions are analysed. Fig. 6(a) shows the schematic cross-section of the Si based NIR phototransistors. The Si substrate also serves as the back gate. Fig. 6(b) shows the band structures of Ti (electrodes) and Si (channel), respectively. All the parameters related to the band gaps and work functions of the materials are extracted from a previous report.[33] The Schottky barrier height between Ti and Si is much lower than the band gap of Si, providing the possibility of hot hole injection across the barrier into the valence band. For gold, the generated hot holes are more energetic (~2 eV) than hot electrons. As a result, only hot hole injection is considered at the p-type Si/Au interface.[25,34] The hot hole generation and migration of p-Si/Au induced by SPP are illustrated in Fig. 6(c). Firstly, the incident wave is localized by the subwavelength structure, and a surface transverse wave with a high ω_p (angular frequency of surface plasmon polariton) will be generated. Free electrons existing at the metal surface will resonate with this localized surface wave. Therefore, the energy of the electromagnetic field is effectively transferred to the free electrons, resulting in the generation of the hot electron–hole pairs. Finally, all the holes have sufficient energy to inject into the semiconductor, *i.e.*, Si. The electrons get motion energy to implement the radiative decay.[35] Hence, under a floating gate (*i.e.*, without a gate bias), the photocurrent will be enhanced because of the increase in the hole concentration in the p-type Si nanomembrane.

For a transistor with a p-type channel, the working principle can be described as follows. When the applied back gate voltage is positive ($V_G > 0$), more and more electrons will be driven and accumulate at the interface of the p-type Si/SiO_2. Therefore, the Fermi level will decrease, leading to a good conductance between the source and the drain. If $V_G \gg 0$, the conduction channel will be inversed into an n-type with an electron dominated conduction, as shown in Fig. 6(d). As a negative bias ($V_G < 0$) is applied at the back gate, holes would be driven to the interface of Si/SiO_2, resulting in an enhanced Fermi level as shown in Fig. 6(e). The negative cut-off region relies on the leakage current with hole as the dominant conduction. On the basis of n-channel electron conduction, hot hole injection induced by SPP resonance will affect the carrier concentration and cause the recombination, as shown in Fig. 6(f).[36–38] On the one hand, the carrier concentration under a positive gate voltage would decrease due to the hot hole injection and recombination, leading to a decreased on-state current, as demonstrated in Fig. 5(d). On the other hand, the carrier concentration under a negative gate voltage would increase due to the hot hole injection, inducing an increased cut-off current, as shown in Fig. 6(g). The reduced threshold can be estimated by the equation, $\Delta V_{Th} = (\Delta N_h \times e)/C_i$, where C_i is the capacitance per unit area of the dielectric layer, ΔV_{Th} is the shift of the threshold voltage, ΔN_h is the reduced hole concentration, and e is the elementary charge.[32,39] Hence, the threshold voltage gradually decreases with the reduced hole concentration, which is in agreement with the results displayed in Fig. 5(f). The detailed explanation and threshold

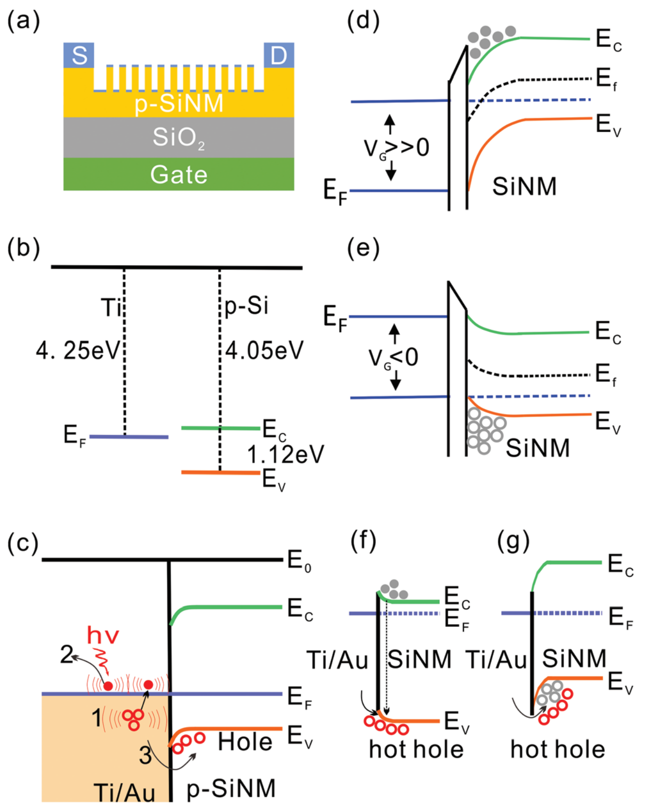

Fig. 6 The mechanism of p-type Si nanomembrane based phototransistors with nanogroove decorated channel and SPP induced hot hole injection. (a) The schematic structure of the phototransistor. (b) Schematic diagram of the energy band structures of Ti and p-type Si. (c) Schematic illustration of the hot carrier loss and injection processes induced by SPP. (d) Schematic energy band alignment and carrier concentration of Si/SiO_2 interface under $V_{gate} \gg 0$. (e) Schematic energy band alignment and carrier concentration of Si/SiO_2 interface under $V_{gate} < 0$. (f) Energy band and carrier recombination between Ti/Au and Si nanomembranes under $V_{gate} \gg 0$. (g) Energy band and carrier recombination between Ti/Au and Si nanomembranes under $V_{gate} < 0$.

voltage shift with increasing incident light power are shown in ESI.† Consequently, SPP induced Si NIR photodetectors with a transistor structure exhibit distinct photoresponse compared with that of a photodiode, which can be theoretically designed and practically applied for high-performance photodetections.

Conclusions

In summary, we demonstrate the infrared photodetection with Si nanomembranes by introducing subwavelength nanogroove structure, which induces the SPP resonance between the incident light and Si, extending the light absorption to the infrared range. Due to the hot hole injection, the I_{on}/I_{off} reaches about 100 when the photodetector is set with a floating gate. On the other hand, if the phototransistor works at the on-state by gate modulation, the electrons of n-type channel are consumed by the hot hole injection, resulting in a negative photo conductance with the photodetection ability (defined as I_{off}/I_{on}) of 6×10^2. Qualitative analysis and theoretical modelling about the mechanism of SPP resonance and hot hole injection help in understanding and designing Si-based NIR photodetectors, which offers guidelines for NIR photodetection using a chip as well as other SPP-related optoelectronics.

Experimental

Fabrication of Si nanomembrane based device with nanogrooves

The fabrication process of Si nanomembrane based NIR photodetectors begins with defining nanostructures in Si materials. A cleaned Si on insulator (SOI, resistivity: 10 Ω cm) with a p-type, 200 nm-thick top Si nanomembrane, the native oxide layer of which is removed by 5% HF solution, is patterned into nanogroove structures. The PMMA (polymethyl methacrylate) is spin coated on the cleaned SOI at an initial rate of 600 rpm for 6 s and a stable rate of 2000 rpm for 50 s. The thickness of the formed PMMA layer is about 1 μm. Then, EBL (electron beam lithography) is performed on the sample to define the etching window. For each unit of nanogroove array, the area is defined as 85 μm × 100 μm. After patterning the sample by RIE (35 sccm SF_6, 18 sccm CHF_3, 30 mT chamber pressure, and 50 W power for 120 s), 2 nm Ti and 15 nm Au are deposited by magnetron sputtering to get smooth and compact absorption objects. Similar photolithography, RIE, and metal deposition process define the bottom electrode of the device. In the present work, we designed the nanogroove with the width a changing from 325 to 470 nm. For all the nanogrooves with different widths, the depth h and period constant d were kept as 180 and 500 nm, respectively.

Morphology characterizations

Surface morphologies of the samples were obtained by atomic force microscopy (AFM, Dimension ICON), SEM (Zeiss Sigma 300, with an operating voltage of 5 kV), and TEM (JEM-ARM300F, with an operating voltage of 100 kV).

Optical characterization

Optical characteristics are carried out by the Fourier transform infrared spectrometer.

Electrical characterizations

Electrical properties of devices are carried out by a semiconductor parameter analyzer (Keithley 4200) at a sweeping voltage of ±2 V under dark and light conditions. A 1550 nm laser with intensity varying in the range of 4 to 168 mW cm^{-2} was used for the photoelectrical measurements. The spectral response of the photodetector was measured by using a series of super-continuum source in the range of 770–1450 nm (YSL Photonics SC-PRO). All the measurements were done after the exposure of the device to the atmosphere under ambient conditions.

FEM simulation

The absorption of nanogroove structured Si nanomembranes under a normal incident plane light source is simulated by using a finite element method. All the geometries and dimensions used in the simulation are in agreement with the experimental data. The periodic boundary conditions are utilized in the perpendicular detection of source incident direction. The distribution of the near-field electric field intensity is obtained through the established monitor.

Conflicts of interest

The authors declare no competing financial interest.

Acknowledgements

The authors thank the financial support from National Natural Science Foundation of China under Grant (No. 51602056 and U1632115), Science and Technology Commission of Shanghai Municipality (17JC1401700 and 18ZR1405100), the National Key Technologies R&D Program of China (2015ZX02102-003), and Program of Shanghai Academic Research Leader (19XD1400600) and the Changjiang Young Scholars Program of China. Part of the experimental work has been carried out in Fudan Nanofabrication Laboratory.

Notes and references

1 Y. Tong, C. Chow, G. Chen, C. Peng, C. Yeh and H. K. Tsang, *IEEE Photonics J.*, 2019, **11**, 1.
2 M. Ko, J. Youn, M. Lee, K. Choi, H. Rucker and W. Choi, *IEEE Photonics Technol. Lett.*, 2012, **24**, 1112.
3 W. Zhou, Z. Ma, S. Chuwongin, Y. Shuai, J. Seo, D. Zhao, H. Yang and W. Yang, *Opt. Quantum Electron.*, 2012, **44**, 605.
4 L. Chen and M. Lipson, *Opt. Express*, 2009, **17**, 7901.
5 H. Chen, M. Galili, P. Verheyen, P. De Heyn, G. Lepage, J. De Coster, S. Balakrishnan, P. Absil, L. Oxenlowe, J. Van Campenhout and G. Roelkens, *J. Lightwave Technol.*, 2017, **35**, 722.
6 A. Karar, N. Das, C. L. Tan, K. Alameh, Y. T. Lee and F. Karouta, *Appl. Phys. Lett.*, 2011, **99**, 133112.
7 S. Latif, S. E. Kocabas, D. A. B. Miller, L. Tang, K. C. Saraswat, A. K. Okyay and D. Ly-Gagnon, *Photonics*, 2008, **2**, 226.
8 C. Tseng, S. Chou, S. Lin, C. Chen, W. Lin, Y. Chen, T. Chung and M. Wu, *J. Vac. Sci. Technol., B: Microelectron. Nanometer Struct.–Process., Meas., Phenom.*, 2008, **26**, 1830.
9 Q. Guo, Z. Di, M. G. Lagally and Y. Mei, *Mater. Sci. Eng., R*, 2018, **128**, 1.
10 E. Song, R. Li, X. Jin, H. Du, Y. Huang, J. Zhang, Y. Xia, H. Fang, Y. K. Lee, K. J. Yu, J. Chang, Y. Mei, M. A. Alam, Y. Huang and J. A. Rogers, *ACS Nano*, 2018, **12**, 10317.
11 E. Song, Y. K. Lee, R. Li, J. Li, X. Jin, K. J. Yu, Z. Xie, H. Fang, Y. Zhong, H. Du, J. Zhang, G. Fang, Y. Kim, Y. Yoon, M. A. Alam, Y. Mei, Y. Huang and J. A. Rogers, *Adv. Funct. Mater.*, 2018, **28**, 1702284.
12 A. Sobhani, M. W. Knight, Y. Wang, B. Zheng, N. S. King, L. V. Brown, Z. Fang, P. Nordlander and N. J. Halas, *Nat. Commun.*, 2013, **4**, 1643.
13 H. Xu, X. Han, X. Dai, W. Liu, J. Wu, J. Zhu, D. Kim, G. Zou, K. A. Sablon, A. Sergeev, Z. Guo and H. Liu, *Adv. Mater.*, 2018, **30**, 1706561.
14 J. Deng, Z. Guo, Y. Zhang, X. Cao, S. Zhang, Y. Sheng, H. Xu, W. Bao and J. Wan, *IEEE Electron Device Lett.*, 2019, **40**, 423.
15 T. Baehr-Jones, M. Hochberg and A. Scherer, *Opt. Express*, 2008, **16**, 1659.
16 Z. Ni, L. Ma, S. Du, Y. Xu, M. Yuan, H. Fang, Z. Wang, M. Xu, D. Li, J. Yang, W. Hu, X. Pi and D. Yang, *ACS Nano*, 2017, **11**, 9854.
17 F. Wang and N. A. Melosh, *Nat. Commun.*, 2013, **4**, 2728.
18 K. Lin, H. Chen, Y. Lai and C. Yu, *Nat. Commun.*, 2014, **5**, 4288.
19 W. Li and J. Valentine, *Nano Lett.*, 2014, **14**, 3510.
20 T. Matsui, Y. Li, M. M. Hsu, C. Merckling, R. F. Oulton, L. F. Cohen and S. A. Maier, *Adv. Funct. Mater.*, 2018, **28**, 1705829.
21 X. Liu, J. Gao, H. Yang, X. Wang and J. Zhao, *Opt. Express*, 2016, **24**, 25103.
22 Y. Sakurai, M. Itou, B. Barbiellini, P. E. Mijnarends, R. S. Markiewicz, S. Kaprzyk, J. M. Gillet, S. Wakimoto, M. Fujita, S. Basak, Y. J. Wang, W. Al-Sawai, H. Lin, A. Bansil and K. Yamada, *Science*, 2011, **332**, 698.
23 J. R. M. Saavedra, A. Asenjo-Garcia and F. J. García De Abajo, *ACS Photonics*, 2016, **3**, 1637.
24 W. H. Weber and G. W. Ford, *Opt. Lett.*, 1981, **6**, 122–124.
25 J. S. DuChene, G. Tagliabue, A. J. Welch, W. Cheng and H. A. Atwater, *Nano Lett.*, 2018, **18**, 2545.
26 B. Y. Zheng, H. Zhao, A. Manjavacas, M. McClain, P. Nordlander and N. J. Halas, *Nat. Commun.*, 2015, **6**, 8797.
27 S. I. Bozhevolnyi, V. S. Volkov, E. Devaux and T. W. Ebbesen, *Phys. Rev. Lett.*, 2005, **95**, 46802.
28 F. J. Garcia-Vidal, L. Martín-Moreno and J. B. Pendry, *J. Opt. A: Pure Appl. Opt.*, 2005, **7**, S97.
29 G. J. Li, Q. L. Guo, Y. F. Fang, S. W. Tang, M. J. Liu, G. S. Huang and Y. F. Mei, *Phys. Status Solidi A*, 2017, **214**, 1700295.
30 A. V. Zayats, I. I. Smolyaninov and A. A. Maradudin, *Phys. Rep.*, 2005, **408**, 131–314.
31 J. Zhu, G. Zhang, J. Wei and J. Sun, *Appl. Phys. Lett.*, 2012, **101**, 123117.
32 Y. Gao, Y. Yi, X. Wang, H. Meng, D. Lei, X. F. Yu, P. K. Chu and J. Li, *Adv. Mater.*, 2019, **31**, 1900763.
33 P. Feng, G. Wu, O. G. Schmidt and Y. F. Mei, *Appl. Phys. Lett.*, 2014, **105**, 121101.
34 R. Sundararaman, P. Narang, A. S. Jermyn, W. A. Goddard III and H. A. Atwater, *Nat. Commun.*, 2014, **5**, 6788.
35 W. Li and J. G. Valentine, *Nanophotonics*, 2017, **6**, 177–191.

36 M. Bernardi, J. Mustafa, J. B. Neaton and S. G. Louie, *Nat. Commun.*, 2015, **6**, 8044.
37 N. N. Esfahani, R. E. Peale, W. R. Buchwald, C. J. Fredricksen, J. R. Hendrickson and J. W. Cleary, *J. Appl. Phys.*, 2013, **114**, 33105.
38 E. A. Shaner, A. D. Grine, M. C. Wanke, M. Lee, J. L. Reno and S. J. Allen, *IEEE Photonics Technol. Lett.*, 2006, **18**, 1925.
39 C. S. Smithson, Y. Wu, T. Wigglesworth and S. Zhu, *Adv. Mater.*, 2015, **27**, 228.